entropy

MDPI

Article

Second Law Analysis of Nanofluid Flow within a Circular Minichannel Considering Nanoparticle Migration

Mehdi Bahiraei * and Navid Cheraghi Kazerooni

Mechanical Engineering Department, School of Energy, Kermanshah University of Technology, Kermanshah 6715685420, Iran; cheraghinavid2015@gmail.com

* Correspondence: m.bahiraei@kut.ac.ir; Tel.: +98-833-7259-980

Academic Editor: Eliodoro Chiavazzo

Received: 19 August 2016; Accepted: 18 October 2016; Published: 21 October 2016

Abstract: In the current research, entropy generation for the water–alumina nanofluid flow is studied in a circular minichannel for the laminar regime under constant wall heat flux in order to evaluate irreversibilities arising from friction and heat transfer. To this end, simulations are carried out considering the particle migration effects. Due to particle migration, the nanoparticles incorporate non-uniform distribution at the cross-section of the pipe, such that the concentration is larger at central areas. The concentration non-uniformity increases by augmenting the mean concentration, particle size, and Reynolds number. The rates of entropy generation are evaluated both locally and globally (integrated). The obtained results show that particle migration changes the thermal and frictional entropy generation rates significantly, particularly at high Reynolds numbers, large concentrations, and coarser particles. Hence, this phenomenon should be considered in examinations related to energy in the field of nanofluids.

Keywords: nanofluid; second law of thermodynamics; entropy generation; particle migration; concentration distribution

1. Introduction

Nanofluids—i.e., suspensions of nanometer-sized particles—are the novel generation of heat transfer fluids for different industrial applications, due to their excellent thermal efficiency. Some instances of the applications of nanofluids include various types of heat exchangers [1,2], thermosyphons and heat pipes [3,4], car radiators [5], cooling of electronic devices, chillers, cooling and heating in buildings, medical applications [6], microchannels [7], and solar collectors [8].

A great deal of research work has been performed on nanofluids [9–11]. The initial studies were mainly confined to measurement and modeling of thermal conductivity. To our knowledge, the first research on these suspensions was implemented in 1993 by Masuda et al. [12]. They added Al_2O_3 and TiO_2 nanoparticles at a concentration of 4.3% in base fluid, and illustrated that the thermal conductivity increment values are 32% and 11%, respectively. In comparison with base fluids, Choi and Eastman [13] showed that the thermal conductivities of Cu–water and carbon nanotube (CNT)–water nanofluids are higher. Eastman et al. [14] indicated that Cu–ethylene glycol nanofluid presents a 40% increment in thermal conductivity at 0.3% concentration.

In spite of the initial studies (which were often done on the thermal conductivity), the researchers have recently paid more attention to the convective heat transfer, since the nanofluids can have many potential applications in the processes associated with convective heat transfer [15–17]. Sundar and Sharma [18] assessed the influence of the water–Al_2O_3 concentration on the Nusselt number and friction factor in a circular pipe having a twisted tape for turbulent condition. Their obtained results showed that the heat transfer augments by concentration and Reynolds number increment.

Mahdavi et al. [19] evaluated flow and heat transfer characteristics of the laminar flow of a nanofluid inside a straight pipe using the Eulerian–Lagrangian method. In this study, some conventional kinds of nanofluids, including nanoparticles of alumina, zirconia, and silica were examined, and the findings were compared with experimental data. Pressure drop predicted by Eulerian–Lagrangian technique was found to be reliable for concentrations less than 3%.

In the research contributions conducted so far, a nanofluid has frequently been presumed to be a uniform suspension which has uniform properties in all positions of the suspension. These assumptions cannot be true, and may lead to mistakes in phenomena associated with nanofluids. In fact, the nanoparticles can have Brownian diffusion resulting from their low mass and size, even if they are in a motionless medium. Therefore, the nanoparticle movement examination is significant to evaluate nanofluids as heat transfer fluids. Additionally, the presented findings on flow and heat transfer features of nanofluids are remarkably inconsistent. These inconsistencies (which are seen to a large extent in the literature) prove that the interactions of base fluid and nanoparticles may considerably affect the amount of heat transfer, and are currently unclear. Although many mechanisms, such as liquid layering, Brownian diffusion, ballistic conduction, etc. have been introduced, there is not any overall approach to demonstrating nanofluid behavior.

A significant parameter that may be operative for the proper characterization of nanofluid behavior is particle migration. It is indicated that if the particle migration impacts are properly considered, more truthful findings that are much closer to the physics of the problem can be achieved. A non-uniform concentration distribution is obtained, caused by the particle migration, which can change the distributions of thermo-physical properties—especially the viscosity and thermal conductivity, as these properties are significantly functions of particle distribution.

Very few research studies have been carried out addressing the impacts of particle migration on the characteristics of nanofluids [20–22]. Ding and Wen [23] examined nanoparticle motion in the flow of nanofluids for the laminar regime. It was found that the particle concentration near the pipe wall is lower in comparison to central areas. Bahiraei [24] examined the hydrothermal properties of the nanofluids containing magnetite nanoparticles for the turbulent regime. The impacts of non-uniform shear rate, Brownian motion, and viscosity gradient were taken into account. By considering the influences of particle migration, the near-wall concentration was smaller than in central areas. The particle concentration non-uniformity was more obvious for the larger nanoparticles, and was augmented by increment of Reynolds number and mean concentration. Malvandi et al. [25] studied heat transfer properties hydromagnetic alumina/water nanofluid through a micro-annulus, taking various mechanisms of particle migration into account. The mode utilized was capable of regarding particle migration due to Brownian diffusion and thermophoresis. The results proved that augmenting the slip velocity and magnetic field improves the heat transfer efficacy, while raising concentration, ratio of internal wall to outer wall radius, and heat flux ratio, reducing thermal efficiency.

Most of the contributions on nanofluids (some of them were mentioned above) have been carried out using the first law of thermodynamics, while it is not properly able to analyze energy saving or wasting alone.

Generally, since the 1970s, the application of the second law of thermodynamics in the thermal design of equipment has attracted substantial attention. The second law of thermodynamics is related to energy availability. The most efficient use of available energy can be attained by applying optimization of thermal exchange equipment through the second law instead of the first law. Employing the second law of thermodynamics has influenced the design approaches of various thermal devices to optimize the rates of entropy production, and therefore to maximize achievable work. The use of one of two terms has been considered by many researchers: irreversibility (entropy generation) and exergy (available energy). Lower entropy production in a piece of thermal equipment means lower energy dissipation. Bejan [26] carried out one of the initial research studies on entropy production for convection heat exchange in a number of important applications. Bejan [27] is the most

famous investigator in this field, and has concentrated on the various factors that are effective on the production of entropy.

Although the key goal in heat exchange systems is the heat exchange rate, the entropy production can be great, which may cause a small efficacy of the second law. Therefore, entropy production analysis could be an appropriate approach to investigating a heat transfer device from a second law viewpoint.

Several researchers have used the second law of thermodynamics in their investigations for the analysis of nanofluid performance. Moghaddami et al. [28] investigated entropy production for two Al_2O_3–water and Al_2O_3–ethylene glycol nanofluids inside a tube under uniform heat flux and for both laminar and turbulent regimes. The authors concluded that the addition of solid nanoparticles decreases entropy production for the laminar regime, whereas there was an optimum Reynolds number in which entropy generation was minimized in turbulent conditions.

Sheremet et al. [29] investigated the influences of a temperature-constant panel insertion for a cavity filled with nanofluid that is chilled using a temperature-constant cooler. The model developed as dimensionless parameters was solved through finite volume approach. The research was carried out for various geometrical ratios of block inserted and temperature-constant cooler, Rayleigh number, and particle concentration. The results showed that Bejan number, Nusselt number, and total entropy generation augment by concentration increment.

Mahian et al. [30] assessed the entropy production between two cylinders, applying TiO_2–water nanofluid under the influence of Magneto-Hydrodynamic (MHD) flow. In addition to the thermal and frictional impacts, the effect of the employed magnetic field on the entropy production was also taken into account. The authors proposed utilizing nanofluids under MHD just for small Brinkman numbers.

Boghrati et al. [31] evaluated entropy production due to the flow of water-based carbon nanotubes (CNTs) and Al_2O_3 nanoparticles inside parallel plates. Between the two plates, a rectangular barrier was situated such that the nanofluid can flow around the barrier. The results revealed that entropy production augments through the addition of solid nanoparticles. Furthermore, it was concluded that the entropy production caused by CNTs is higher than that resulting from Al_2O_3 nanoparticles.

Mahmoudi et al. [32] investigated the effect of MHD on the production of entropy, applying Cu–water nanofluids inside a trapezoidal cavity. It was concluded that the production of entropy decreases as concentration increases, whereas it increases with the magnetic field.

Frictional, thermal, and total entropy generation rates for the water–Al_2O_3 nanofluid flow inside a circular minichannel are examined in the present work, with respect to the particle migration effects. The impacts of parameters such as particle size, Reynolds number, and concentration on entropy production are studied. To the best knowledge of the authors, the current research is the first investigation in which the second law analysis is employed to assess irreversibility in nanofluids with respect to the impacts of particle migration.

2. Particle Migration

This study is conducted on the flow of water–Al_2O_3 nanofluid within a circular minichannel in order to evaluate the irreversibilities caused by friction and heat transfer with respect to the migration of nanoparticles. Three main factors cause the migration of particles in non-uniform shear flows:

- Particle movement from greater shear rate areas to smaller shear rate ones, caused by shear-induced mechanism;
- Particle movement from greater viscosity areas to smaller viscosity ones, due to viscosity gradient;
- Particle movement from higher concentration areas to smaller concentration ones, due to Brownian motion [33–35].

These factors affect particle migration differently. For instance, shear-induced particle migration leads to a concentration of the particles in areas with low shear, whereas Brownian diffusion moves the particles from areas of higher concentration to those with smaller concentration.

Considering mass balance for the solid phase in a nanofluid flow having conditions of steady state and fully developed inside a pipe will present [23]:

$$J + r\frac{\mathrm{d}J}{\mathrm{d}r} = 0 \tag{1}$$

where r represents the radial coordinate and J denotes the total particle flux in the r direction. As mentioned above, the total particle migration flux includes three mechanisms:

$$J = J_\mu + J_c + J_b \tag{2}$$

where J_μ, J_c, and J_b stand for the particle flux resulting from viscosity gradient, particle flux due to non-uniform shear rate, and particle flux caused by Brownian diffusion, respectively. Phillips et al. [34] presented these equations:

$$J_\mu = -K_\mu \dot{\gamma}\varphi^2 \left(\frac{d_p^2}{\mu}\right)\frac{\mathrm{d}\mu}{\mathrm{d}\varphi}\nabla\varphi \tag{3}$$

$$J_c = -K_c d_p^2(\varphi^2\nabla\dot{\gamma} + \varphi\dot{\gamma}\nabla\varphi) \tag{4}$$

$$J_b = -D_b\nabla\varphi \tag{5}$$

where K_μ and K_c denote phenomenological constants, $\dot{\gamma}$ represents the shear rate, φ is the concentration, d_p is the particle size, μ is the dynamic viscosity, and D_b represents the Brownian diffusion coefficient, calculated by:

$$D_b = \frac{k_B T}{3\pi\mu d_p} \tag{6}$$

where k_B represents Boltzmann's constant and T is the temperature.

By integrating Equation (1) and applying boundary condition at $r = 0$, Equation (7) is obtained. In fact, the boundary condition of symmetry at the center of the pipe is employed.

$$J = J_\mu + J_b + J_c = 0 \tag{7}$$

It should be noted that Equation (7) is applicable for all radial locations under the fully developed and steady state condition (not only at the tube center).

Equation (8) is achieved by substituting Equations (3)–(5) into Equation (7):

$$K_\mu\dot{\gamma}\varphi^2\frac{d_p^2}{\mu}\frac{\mathrm{d}\mu}{\mathrm{d}r} + K_c d_p^2\varphi^2\frac{\mathrm{d}\dot{\gamma}}{\mathrm{d}r} + K_c d_p^2\varphi\dot{\gamma}\frac{\mathrm{d}\varphi}{\mathrm{d}r} + D_b\frac{\mathrm{d}\varphi}{\mathrm{d}r} = 0 \tag{8}$$

For a Newtonian fluid:

$$\dot{\gamma} = \frac{1}{2\mu}\left(\frac{\mathrm{d}P}{\mathrm{d}z}\right)r \tag{9}$$

where $\dot{\gamma} = \frac{dv}{dr}$ (v denotes the velocity) and P represents the pressure. The variable z is the longitudinal component. By supposing the nanofluid is a Newtonian fluid, Equation (8) is achieved as below:

$$\frac{1}{\mu}\frac{\mathrm{d}\mu}{\mathrm{d}\bar{r}} + \left(\frac{K_c}{K_\mu}\right)\frac{\mu}{\bar{r}}\frac{\mathrm{d}\left(\frac{\bar{r}}{\mu}\right)}{\mathrm{d}\bar{r}} + \left(\frac{K_c}{K_\mu}\right)\frac{1}{\varphi}\frac{\mathrm{d}\varphi}{\mathrm{d}\bar{r}} - \frac{1}{\varphi^2\bar{r}}\frac{1}{K_\mu Pe}\frac{\mathrm{d}\varphi}{\mathrm{d}\bar{r}} = 0 \tag{10}$$

where

$$\bar{r} = \frac{r}{R}, Pe = \frac{3\pi d_p^3\left(-\mathrm{d}P/\mathrm{d}z\right)R}{2k_B T} \tag{11}$$

The parameter Pe is Peclet number. This dimensionless number presents the ratio of particle migration due to convection to that of Brownian motion. The parameter R denotes the pipe radius.

The following equation [36] was used for the nanofluid effective viscosity in Equation (10).

$$\mu = \mu_f(123\varphi^2 + 7.3\varphi + 1) \tag{12}$$

where subscript f refers to the base fluid.

A boundary condition is needed to solve Equation (10), which is obtained from Equation (13):

$$\varphi_m = \frac{\int \varphi(r)\mathrm{d}A}{\int \mathrm{d}A} \tag{13}$$

where φ_m is the mean concentration and A denotes the area.

Nanoparticle concentration distribution is achieved by solving Equation (10) under various conditions.

3. Governing Equations and Boundary Conditions

The continuity, momentum, and energy equations have been presented in the following, which should be solved by applying effective properties.

Conservation of mass:

$$\frac{1}{r}\frac{\partial(\rho r v_r)}{\partial r} + \frac{\partial(\rho v_x)}{\partial x} = 0 \tag{14}$$

Conservation of momentum:

$$\left(v_r\frac{\partial \rho v_r}{\partial r} + v_x\frac{\partial \rho v_r}{\partial x}\right) = -\frac{\partial P}{\partial r} + \left(\frac{\partial}{\partial r}\left(\frac{\mu}{r}\frac{\partial(r v_r)}{\partial r}\right) + \frac{\partial}{\partial x}\left(\mu\frac{\partial v_r}{\partial x}\right)\right) \tag{15}$$

$$\left(v_r\frac{\partial \rho v_x}{\partial r} + v_x\frac{\partial \rho v_x}{\partial x}\right) = -\frac{\partial P}{\partial x} + \left(\frac{1}{r}\frac{\partial}{\partial r}\left(\mu r\frac{\partial v_x}{\partial r}\right) + \frac{\partial}{\partial x}\left(\mu\frac{\partial v_x}{\partial x}\right)\right) \tag{16}$$

Conservation of energy:

$$\frac{1}{r}\frac{\partial}{\partial r}\left(r\rho c_p T u_r\right) + \frac{\partial}{\partial x}\left(\rho c_p T u_x\right) = \frac{1}{r}\frac{\partial}{\partial r}\left(kr\frac{\partial T}{\partial r}\right) + \frac{\partial}{\partial x}\left(k\frac{\partial T}{\partial x}\right) \tag{17}$$

where ρ represents density, c_p denotes specific heat, and k is thermal conductivity.

3.1. Nanofluid Properties

In the research contributions, in which a single-phase method has been applied to simulate nanofluids, uniform properties have been employed. The effective properties, however, are utilized in the current survey as location-dependent after determining the distribution of concentration. The following models were employed to calculate specific heat and density, whereas Equation (12) was applied to evaluate the viscosity.

$$\rho = \varphi\rho_p + (1-\varphi)\rho_f \tag{18}$$

$$c_p = \frac{(1-\varphi)(\rho c_p)_f + \varphi(\rho c_p)_p}{\rho} \tag{19}$$

where subscript p refers to the nanoparticles.

Furthermore, the model presented by Maiga et al. [36] was employed to evaluate the thermal conductivity:

$$k = k_f(4.97\varphi^2 + 2.72\varphi + 1) \tag{20}$$

It is noteworthy that the location-dependent concentration is applied in above equations.

3.2. Boundary Conditions

At the pipe inlet, developed velocity and uniform temperature are utilized. No-slip condition and constant heat flux are employed on the wall. Moreover, atmospheric static pressure is applied at the pipe outlet.

The boundary conditions are presented mathematically as follows:

- At the inlet of the minichannel ($x = 0$):

$$\mathbf{u} = \mathbf{u}_{developed},\ T = T_0 \tag{21}$$

- At the wall:

$$\mathbf{u} = 0,\ -k\frac{\partial T}{\partial r} = q'' \tag{22}$$

- At the outlet of the minichannel:

$$P = P_0 \tag{23}$$

4. Entropy Generation

Two factors cause local entropy production rate; one of them originates from heat transfer, and other is due to friction. Equation (24) presents the local entropy production rate per unit volume:

$$\dot{S}_t''' = \dot{S}_h''' + \dot{S}_f''' \tag{24}$$

where $\dot{S}_t'''$, $\dot{S}_h'''$ and $\dot{S}_f'''$ represent total, thermal and frictional entropy generation rates, respectively.

$$\dot{S}_h''' = \frac{k}{T^2}\left[\left(\frac{\partial T}{\partial x}\right)^2 + \left(\frac{\partial T}{\partial r}\right)^2\right] \tag{25}$$

$$\dot{S}_f''' = \frac{\mu}{T}\left\{2\left[\left(\frac{\partial v_x}{\partial x}\right)^2 + \left(\frac{\partial v_r}{\partial r}\right)^2\right] + \left(\frac{\partial v_x}{\partial r} + \frac{\partial v_r}{\partial x}\right)^2\right\} \tag{26}$$

By integrating from local entropy production rate as per Equation (27), entropy production rate for total volume of the nanofluid is calculated. Equation (27) is usable for total, frictional, and thermal entropy generation.

$$\dot{S} = \int \dot{S}''' \mathrm{d}V \tag{27}$$

To measure the contributions of two factors which are effective in entropy production, a dimensionless number called the Bejan number is introduced according to Equation (28), which gives the ratio of thermal entropy production rate to the total one. It should be noted that the Bejan number is examined locally as well as globally.

$$Be = \frac{\dot{S}_h'''}{\dot{S}_t'''} \tag{28}$$

5. Numerical Method and Validation

The investigation was performed through a finite volume approach. To solve the equations of momentum and energy, a second order upwind model was used. Moreover, the SIMPLE (Semi-Implicit Method for Pressure-Linked Equations) approach was adopted for coupling the velocity and pressure. The simulation is an axisymmetric problem, and therefore onlyt half of the field was considered two-dimensionally. The diameter of the minichannel was considered to be 1 mm. To finalize the numerical executions, convergence criterion was assumed 10^{-6} for the variables. Besides, to ensure grid independency, several grids were evaluated, and the one having 20×2500 nodes was chosen as the best meshing. Indeed, no considerable change was observed in the findings of smaller meshes.

The findings of grid independency check have been presented in Table 1 for Nusselt number at a dimensionless length of the channel (i.e., x/D = 200).

Table 1. Grid independency study for Nusselt (Nu) number at x/D = 200.

Grid	Nu (Numerical)	Nu (Equation (29))
15 × 800	5.295	5.452
15 × 1000	5.412	5.452
18 × 2000	5.414	5.452
20 × 2500	5.445	5.452
28 × 2900	5.443	5.452

For validation, the results of the present numerical solution were compared with reliable data for pure water as well as nanofluid. Hence, a valid equation for water, and an experimental work for the water–Al_2O_3 nanofluid were applied for investigation of the validity of the method. Equation (29) was utilized for water [37]:

$$Nu = \begin{cases} 3.302x_+^{-1/3} - 1, \ x_+ \leq 0.00005 \\ 1.302x_+^{-1/3} - 0.5, \ 0.00005 \leq x_+ \leq 0.0015 \\ 4.364 + 8.68(10^3 x_+)^{-0.506} e^{-41x_+}, \ x_+ \geq 0.0015 \end{cases} \quad (29)$$

where $x_+ = \frac{x}{DRePr}$ in which Pr denotes the Prandtl number, and D represents the diameter of the pipe.

Figure 1 presents a comparison between the results of the present study and those of Equation (29) for water. It is observed that there is a very good agreement between the results. In addition, the convective heat transfer coefficients achieved from the current study were compared with the experimental data [38] for water–Al_2O_3 nanofluid within a circular tube in Table 2. In this table, a proper consistency is noticed between the data, proving that the solution is valid.

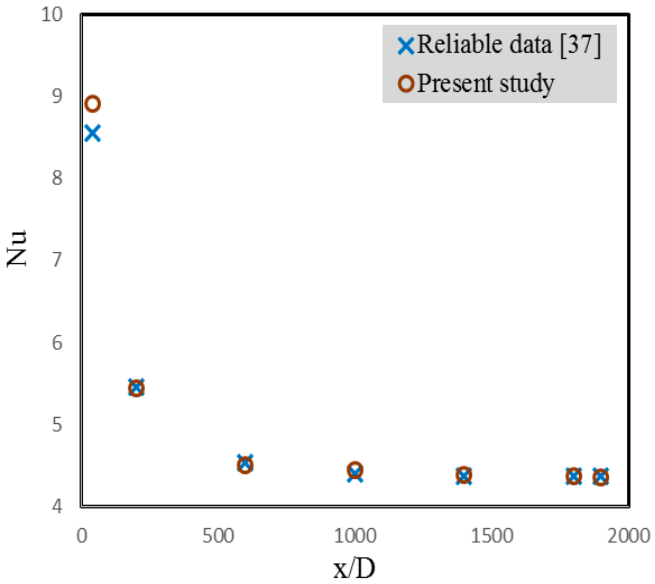

Figure 1. Nusselt number (Nu) obtained from the present work compared to valid data [37] for pure water.

Table 2. Convective heat transfer coefficient obtained from the present study compared to the experimental data [38] for φ = 1% at different Reynolds numbers.

Re	Experimental Results [38]	Present Study (with Particle Migration)	Present Study (without Particle Migration)
300	2555	2604	2637
900	2761	2691	2680
1500	2889	2823	2792
2000	3107	3148	3174

6. Results and Discussion

Numerical research is conducted in order to assess the influence of particle migration on entropy production for the water–Al_2O_3 nanofluid flow within a circular minichannel under a constant wall heat flux (i.e., 5000 W/m^2). The numerical runs are carried out for mean concentrations of 1%, 3% and 5%, the Reynolds numbers of 200, 1000, and 2000, and particle sizes of 10, 50, and 90 nm. For this goal at first, the distribution of the concentration at the cross-section of the pipe should be determined by solving Equation (10) for different states.

Figure 2 depicts the concentration distribution for various mean concentrations at *Re* = 2000 and d_p = 90 nm at a tube cross-section. As can be observed, non-uniformity of the concentration distribution intensifies by mean concentration increment, so that the nanofluid attains a higher concentration in the central areas of the tube. This observation is attributed to $1/\varphi^2$ in the latest term of Equation (10), which considerably reduces with the increase of concentration, due to the power of second order in the denominator. Indeed, the impact of Brownian motion—which tends to make the particle distribution more uniform—reduces by the concentration increment as compared to the effect of the other factors.

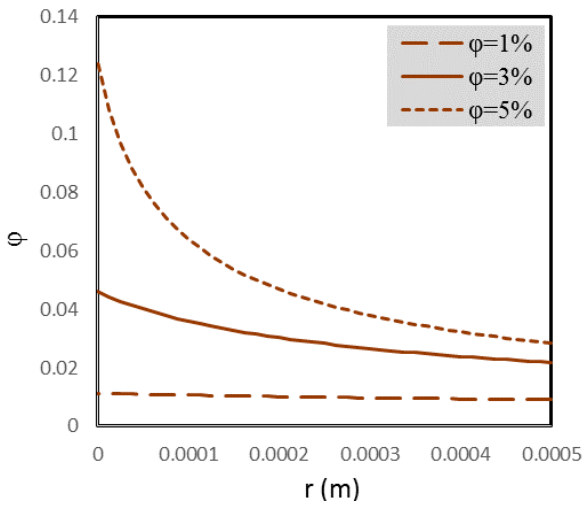

Figure 2. Concentration distribution at a cross-section of the tube for different mean concentrations at *Re* = 2000 and d_p = 90 nm.

The concentration distribution is presented in Figure 3 for different Reynolds numbers at φ_m = 5% and d_p = 90 nm. It can be noticed that augmenting the Reynolds number makes the concentration distribution rather non-uniform at the tube cross-section. This is attributed to an increment in diffusion due to non-uniform shear induced at the higher Reynolds numbers, which can increase gathering of the nanoparticles in the central areas.

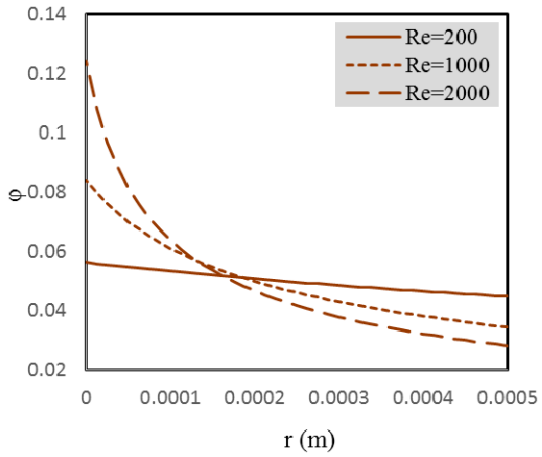

Figure 3. Concentration distribution for different Reynolds numbers at φ_m = 5% and d_p = 90 nm.

The concentration distribution at the tube cross-section is illustrated in Figure 4 for different sizes of the nanoparticles at Re = 2000 and φ_m = 5%. As can be observed, the concentration distribution becomes more non-uniform by particles' enlargement. The non-uniform shear rate leads to the migration of nanoparticles to the central areas of the tube, while the Brownian diffusion guides the nanoparticles opposite to the concentration gradient. Thus, these two mechanisms work in two opposite directions. By increasing the particle size, the impact of the Brownian diffusion reduces, while the influence of the non-uniform shear rate augments. Thus, at a given mean concentration, a higher agglomeration of the nanoparticles accumulates in the central areas for coarser nanoparticles, such that the concentration value increases just 0.36% from the wall to the tube center for the particles of 10 nm size, while it increases by almost four times from the wall to the tube center for particles of 90 nm size.

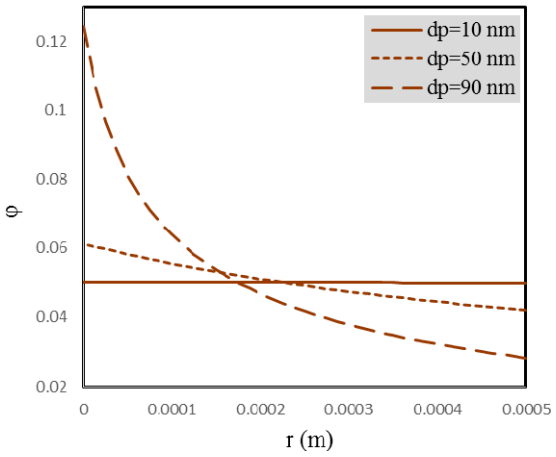

Figure 4. Concentration distribution at the tube cross-section for different sizes of nanoparticles at Re = 2000 and φ_m = 5%.

The effects of various parameters on entropy production rates will be discussed in the following, taking into consideration the particle migration impacts. Local investigations are carried out on a cross-section of 0.9 m distance from the tube inlet, unless otherwise mentioned for the relevant cross-section location.

Figure 5 illustrates the thermal entropy generation rate at Re = 2000 and d_p = 90 nm for various concentrations. As seen from this figure, increasing the concentration leads to a reduction in the thermal entropy production. The reason for this is that the increased concentration improves the nanofluid

thermal conductivity, which results in a reduction of the temperature gradient (see Figures 6 and 7). On the other hand, the greater concentration increases the nanofluid viscosity, and because the investigations are done at a constant Reynolds number, the nanofluid velocity shall be augmented (since the viscosity is in the Reynolds number denominator), which causes a nanofluid temperature decrement. The lower temperature enhances the thermal entropy generation rate because the temperature is located in the denominator of the equation, which describes the thermal entropy generation (Equation (25)). However, since the temperature gradient decrease dominates the temperature decrease, the thermal entropy generation rate reduces with concentration augmentation.

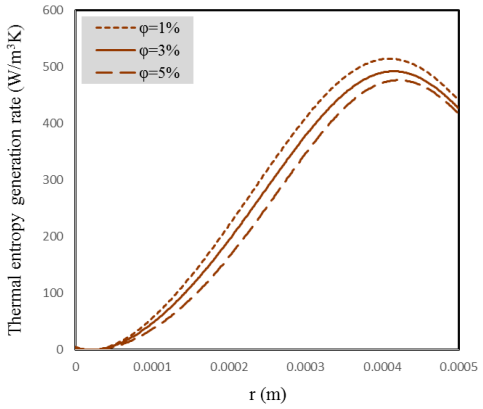

Figure 5. Thermal entropy generation rate for different concentrations at Re = 2000 and d_p = 90 nm.

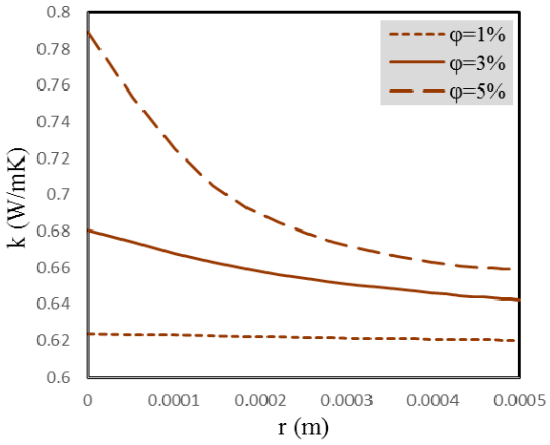

Figure 6. Thermal conductivity at a tube cross-section for different concentrations.

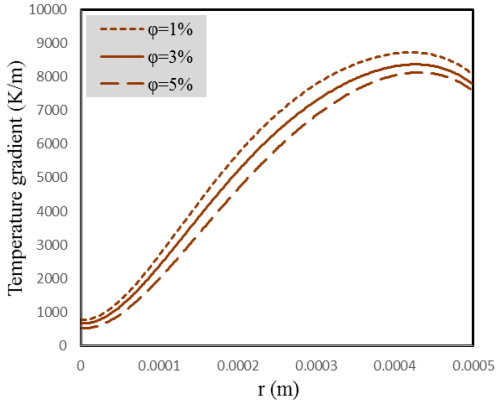

Figure 7. Temperature gradient at a tube cross-section for different concentrations.

Figure 8 shows the distributions of thermal entropy generation rate for two different cross-sections—one just close to the inlet (i.e., at x = 0.05 m), and the other close to the outlet (i.e., at x = 0.9 m)—at Re = 2000, d_p = 90 nm, and φ_m = 5%. It is clearly seen that at the cross-section near the inlet, the thermal entropy generation rate is insignificant in a wide area of this cross-section. The reason for this is that the temperature gradient is negligible in the central areas because the thermal boundary layer has not developed much, and has not yet reached central regions as a consequence. However, at the cross-section near the outlet, this rate has become significant in a wider area of the cross-section due to more development of the thermal boundary layer. In addition, it is noticed that the thermal entropy production rate near the wall for the cross-section close to the outlet is smaller than that for the one close to the inlet. The reason is that on one hand, the temperature gradient on the wall is the same for both of the cross-sections, in accordance with the Fourier law (Equation (30)), and on the other hand, for the cross-section close to the outlet, the temperature is higher, and consequently, the thermal entropy generation near the wall for this cross-section will be smaller (as per Equation (25)).

$$q'' = k\frac{\partial T}{\partial r} \tag{30}$$

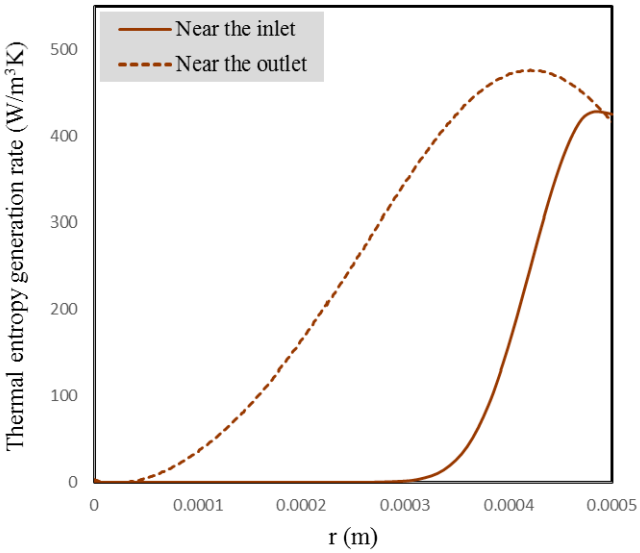

Figure 8. Profiles of thermal entropy generation rate at two different cross-sections for Re = 2000, d_p = 90 nm, and φ_m = 5%.

Figure 9 illustrates the frictional entropy generation rate at Re = 2000 and d_p = 90 nm for various concentrations. Increasing the concentration intensifies the frictional entropy production rate. One reason is that the nanofluid viscosity increases at higher concentrations (see Figure 10a), which can increase the frictional entropy generation rate (as per Equation (26)). On the other hand, since the examination is done at a constant Reynolds number, and the viscosity—which is in denominator of the Reynolds number calculation—increases by increasing the concentration, greater velocities are adopted at higher concentrations (see Figure 10b), which can augment the frictional entropy generation due to the velocity gradient increment. Another reason for the increased frictional entropy generation rate at higher concentrations is that the nanofluid temperature decreases by concentration augmentation (see Figure 10c). The reason for the temperature reduction is that although the nanofluid specific heat decreases at greater concentrations (and the specific heat decrement can increase the nanofluid temperature), the increased velocity compensates for this specific heat reduction, such that the temperature eventually decreases. Thus, since the temperature is in the denominator of Equation (26), the temperature reduction can increase the frictional entropy generation rate. Additionally, due to the more intensive particle migration to the central areas at higher

concentrations (and thus, more non-uniform distribution of the concentration at the cross-section of the pipe), the nanofluid viscosity reduces considerably near the wall, which can intensify the velocity gradient there (see Figure 11). As shown in Figure 9, this causes significant discrepancy in the frictional entropy generation rates adjacent to the wall for different concentrations.

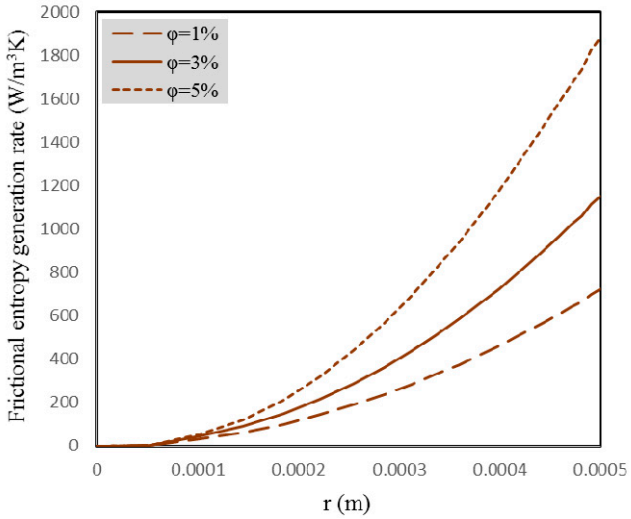

Figure 9. Frictional entropy generation rate for different concentrations at Re = 2000 and d_p = 90 nm.

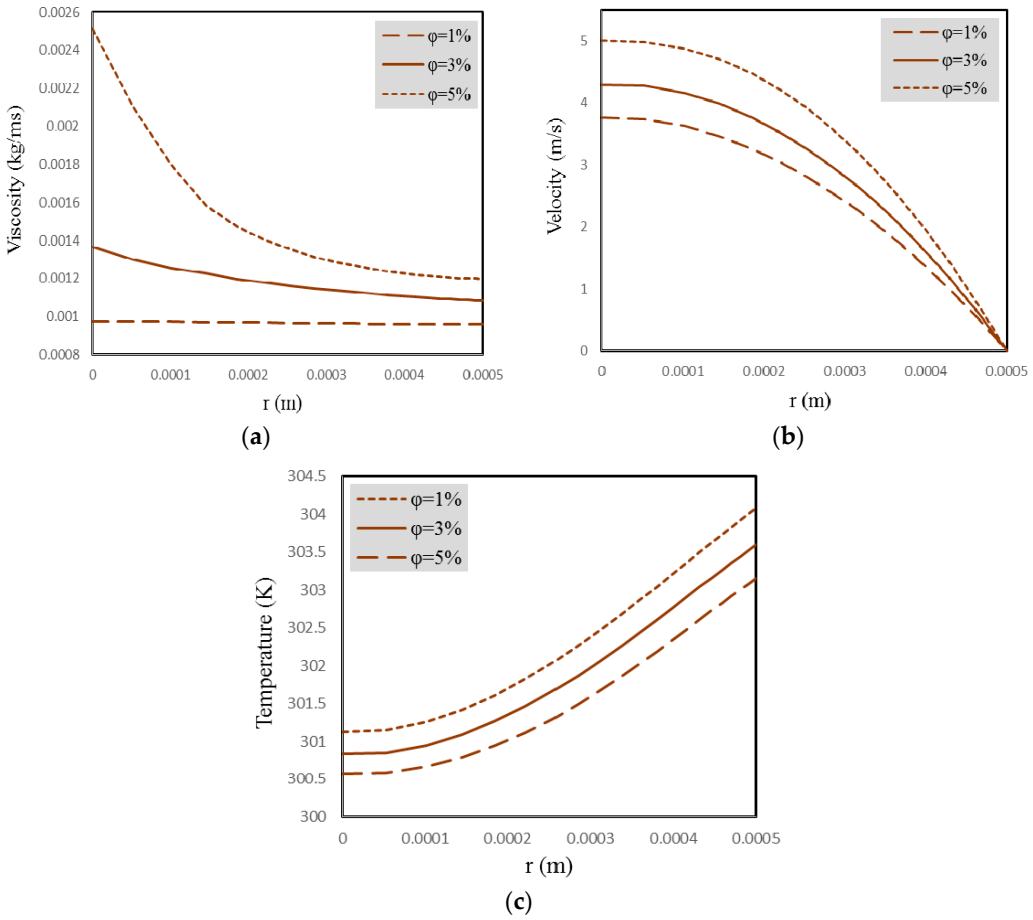

Figure 10. Effect of concentration change at Re = 2000 and d_p = 90 nm on: (**a**) viscosity; (**b**) velocity; (**c**) temperature.

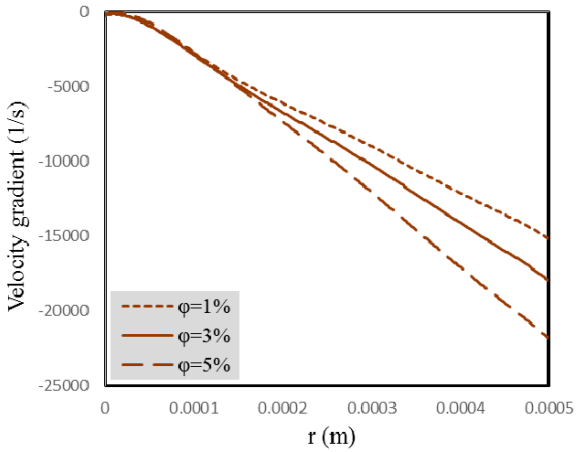

Figure 11. Velocity gradient at tube cross-section for different concentrations.

The total entropy generation rate versus the concentration is illustrated in Figure 12 for Re = 2000 and d_p = 90 nm. It is noticed that variations of the total entropy generation rate at the concentrations of 3% and 5% have a similar trend to those of the frictional entropy generation rate. This is because the contribution of the frictional entropy generation is much greater than that of the thermal entropy generation at these concentrations, as is evident from a comparison between Figures 5 and 9. However, at the concentration of 1%, the frictional and thermal entropy generation rates have close values; therefore, the trend of variations in the total entropy generation rate at this concentration is affected by both thermal and frictional entropy generation rates.

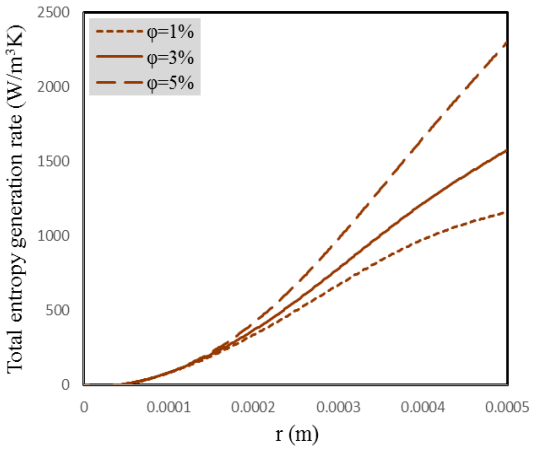

Figure 12. Total entropy generation rate in terms of the concentration at Re = 2000 and d_p = 90 nm.

Figure 13 depicts the thermal entropy generation rate for different Reynolds numbers at φ_m = 5% and d_p = 90 nm. It is seen that the thermal entropy generation rate near the wall is greater at the larger Reynolds numbers. This is because at greater Reynolds numbers (as discussed before, Figure 3), migration of the particles to the central areas occurs with more intensity, so that the concentration decreases more significantly near the wall. This causes a decrease of the thermal conductivity adjacent to the wall at the higher Reynolds numbers. Therefore, with respect to the constant amount of heat flux on wall, the temperature gradient at the vicinity of the wall will be greater at larger Reynolds numbers (see Figure 14). Approaching the central regions, the opposite trend is noted. In other words, for higher Reynolds numbers at the central regions, the thermal conductivity increases; consequently, the temperature gradient decreases in comparison with lower Reynolds numbers. This will reduce the thermal entropy production rate in the central areas at higher Reynolds numbers.

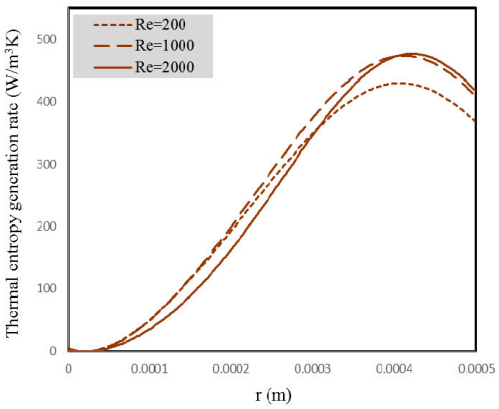

Figure 13. Thermal entropy generation rate for different Reynolds numbers at φ_m = 5% and d_p = 90 nm.

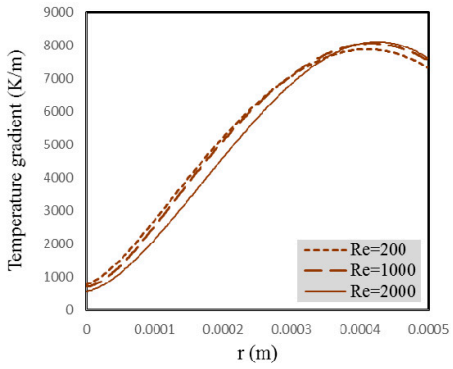

Figure 14. Temperature gradient for different Reynolds numbers at φ_m = 5% and d_p = 90 nm.

Frictional entropy generation rate is demonstrated in Figure 15 for different Reynolds numbers at φ_m = 5% and d_p = 90 nm. As is clearly seen from this figure, the frictional entropy generation rate increases at the higher Reynolds numbers. The difference between the frictional entropy generation rates becomes more considerable near the wall. One can notice from Figure 16 that increasing the Reynolds number has a significant effect on the velocity gradient intensification. Here, in addition to the effect of velocity increase on velocity gradient increment, the concentration distribution is more non-uniform at greater Reynolds numbers (Figure 3). This will reduce the viscosity near the wall, and therefore the gradient of the velocity will be more significant there; finally, it causes a significant discrepancy between the frictional entropy generation rates near the wall for different Reynolds numbers.

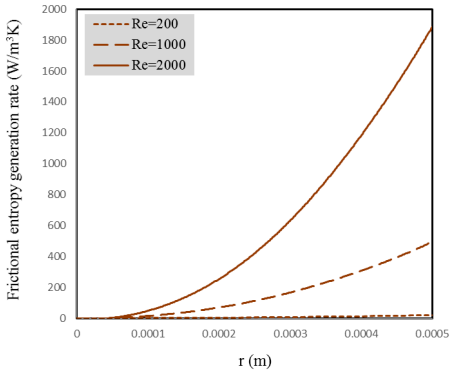

Figure 15. Frictional entropy generation rate for different Reynolds numbers at φ_m = 5% and d_p = 90 nm.

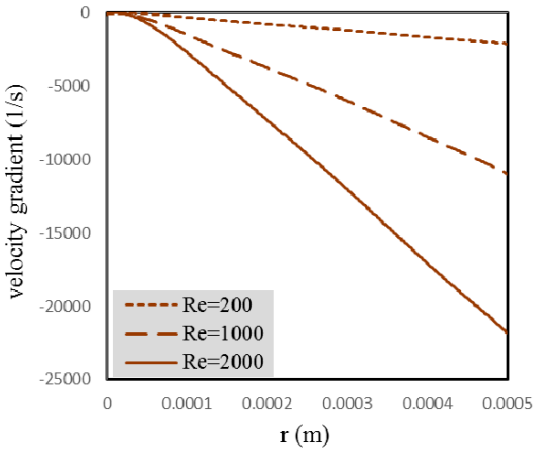

Figure 16. Velocity gradient for different Reynolds numbers at φ_m = 5% and d_p = 90 nm.

Figure 17 shows the total entropy generation rate at φ_m = 5% and d_p = 90 nm for various Reynolds numbers. As can be noticed, the diagram of the total entropy generation rate at Re = 2000 is very like that of the frictional entropy generation rate. This is because at this Reynolds number (as is obvious in Figures 13 and 15), the frictional entropy generation has a significantly greater contribution compared to the entropy generation due to heat transfer. At Re = 1000, wherein the contributions of the friction and heat transfer in entropy generation are almost equal, the diagram of the total entropy generation rate has been affected by both factors equally. However, the thermal entropy generation completely dominates the frictional entropy generation at Re = 200, and that is why the diagram of the total entropy generation rate in Figure 17 is to a large extent similar to the thermal entropy production rate.

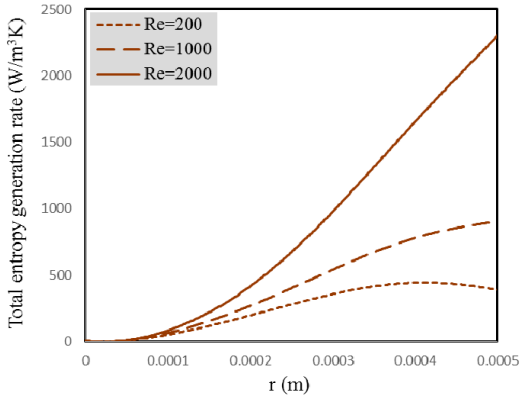

Figure 17. Total entropy generation rate for different Reynolds numbers at φ_m = 5% and d_p = 90 nm.

Figure 18 depicts the impact of particle size on thermal entropy generation rate at φ_m = 5% and Re = 2000. It is observed that the thermal entropy generation rate near the wall intensifies by an increase of the nanoparticle size. Going far from the wall and approaching to the tube center, the opposite trend is observed, where an increase in the nanoparticle size corresponds to a smaller thermal entropy generation rate in the central regions. This is because, in accordance with Equation (11), as the nanoparticle size increases, the Peclet number will be greater, which intensifies migration of the nanoparticles to the central regions. As a consequence, the concentration distribution will be more non-uniform at the tube cross-section (Figure 4). For larger particles, the concentration will thus be lower adjacent to the wall, and higher in the central areas. This can reduce the thermal conductivity in regions adjacent to the wall, and enhance it in the central areas. Thus, for larger nanoparticles, the temperature gradient augments at the wall vicinity and reduces in the central areas.

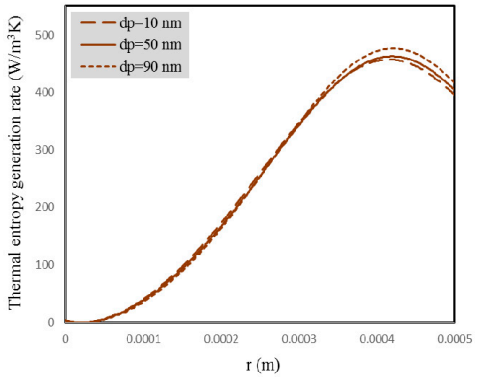

Figure 18. Effect of nanoparticle size on thermal entropy generation rate at φ_m = 5% and Re = 2000.

Figure 19 displays the frictional entropy generation rate at φ_m = 5% and Re = 2000 for various particle diameters. It is observed that the frictional entropy generation rate reduces with increasing nanoparticle size. For larger nanoparticles, although the velocity gradient is greater adjacent to the wall (Figure 20), the frictional entropy generation rate is lower. The reason for this is that for the larger nanoparticles, the viscosity becomes smaller near the wall due to more considerable particle migration toward the central areas (see Figure 21). Meanwhile, the velocity gradient decreases in the central regions due to the velocity profile flattening for the greater nanoparticles, due to the viscosity increment. This reduction in the velocity gradient will decrease the frictional entropy generation rate there when compared against the case using finer particles.

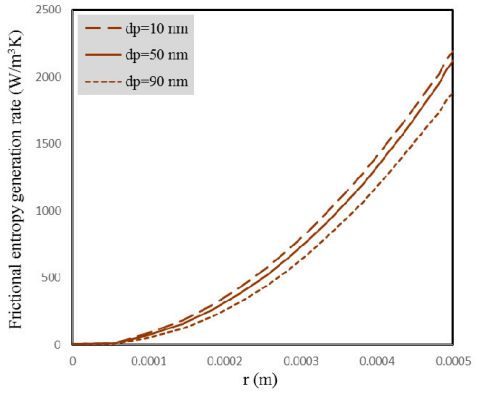

Figure 19. Frictional entropy generation rate at φ_m = 5% and Re = 2000 for different particle sizes.

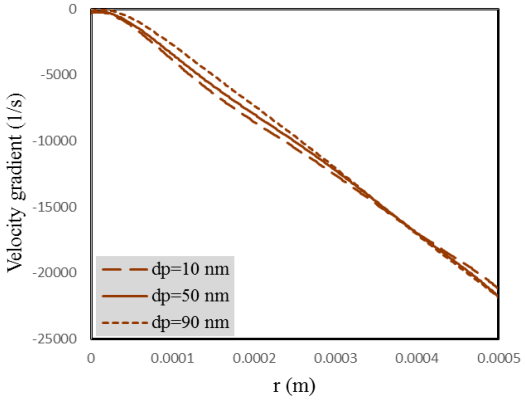

Figure 20. Velocity gradient at different particle sizes.

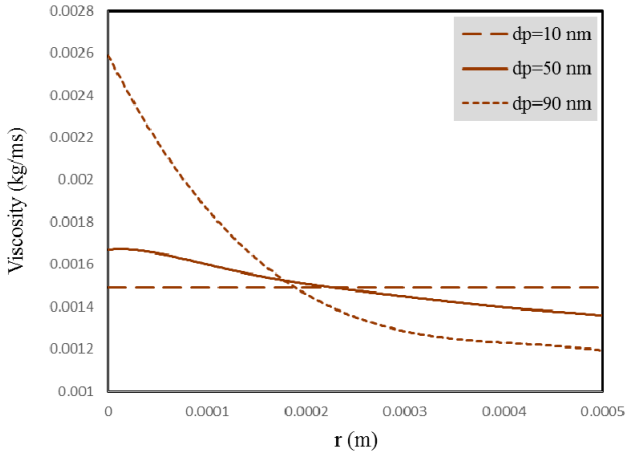

Figure 21. Nanofluid viscosity at different particle sizes.

Figure 22 illustrates the total entropy production rate for various nanoparticle sizes at φ_m = 5% and Re = 2000. It is noticed that in all particle sizes, the total entropy generation rate changes with a trend that is similar to that of the frictional entropy production rate. This is attributed to the greater contribution of the frictional entropy production compared to that of the thermal entropy generation at Re = 2000 and φ_m = 5% (see Figures 18 and 19). Furthermore, it is noticed that an increase of the nanoparticle size decreases the total entropy production rate, such that the total entropy production rate decreases by about 20% on average by increasing the particle size from 10 to 90 nm.

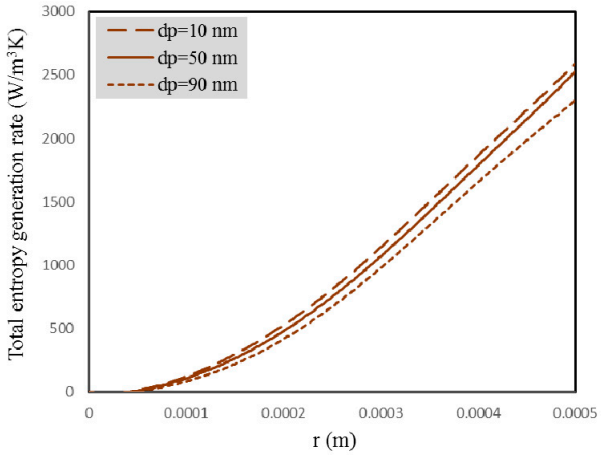

Figure 22. Total entropy generation rate for different nanoparticle sizes at φ_m = 5% and Re = 2000.

The Bejan number is employed to determine the contribution of two factors in entropy production (i.e., friction and heat transfer). Figure 23 depicts the local Bejan number at φ_m = 5% and Re = 2000 for various particle sizes. As can be noticed, the Bejan number is higher than 0.5 in the central regions, and consequently, the contribution of the thermal entropy generation is greater than that of the frictional one. Nevertheless, near the wall, the trend is opposite, and since the Bejan number is smaller than 0.5, the contribution of frictional entropy production is higher than that of the thermal entropy generation. Furthermore, looking at this figure will reveal that as the particles increase in size, the Bejan number changes from values over 0.5 to values below 0.5, occurring further away from the centerline. The reason for this is attributed to the rather non-uniform concentration distribution for the larger nanoparticles.

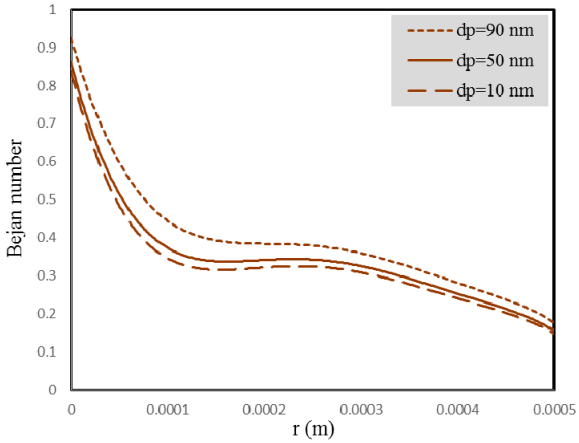

Figure 23. Local Bejan number for different particle sizes at φ_m = 5% and Re = 2000.

Up to here, the effects of particle size, Reynolds number, and particle concentration on the rate of entropy production were assessed considering particle migration. In most of the papers available in the related literature, nanofluids have been considered as homogeneous fluids with uniform concentration distribution. The effect of regarding the phenomenon of nanoparticle migration is studied in the following on the generation of entropy in the nanofluid as compared to the state in which the migration of nanoparticles is not taken into account at all. In the following investigations, the non-uniform model means regarding the impact of particle migration, which causes concentration gradients, and thus, the non-uniform distribution of thermophysical properties at the cross-section of the tube. In addition, the uniform model means ignoring the particle migration, the result of which would be a uniform concentration distribution, and therefore, uniform thermophysical properties throughout the domain.

Figure 24 shows the rate of thermal entropy generation for two uniform and non-uniform models at φ_m = 5%, Re = 2000, and d_p = 90 nm. As can be observed, the thermal entropy production rate for the non-uniform model is greater than that for the uniform one near the wall. This is due to migration of the particles, which reduces the concentration there. Therefore, the thermal conductivity will also be smaller in this region, and the temperature gradient increases due to the wall heat flux being constant (see Equation (30)). It is also noticed that the effect of considering the particle migration near the wall is higher than that in the central regions. Furthermore, in the central areas, the thermal entropy production rate for the case of considering the particle migration is smaller in comparison with the result obtained from the uniform model, since the concentration is greater for the non-uniform model there.

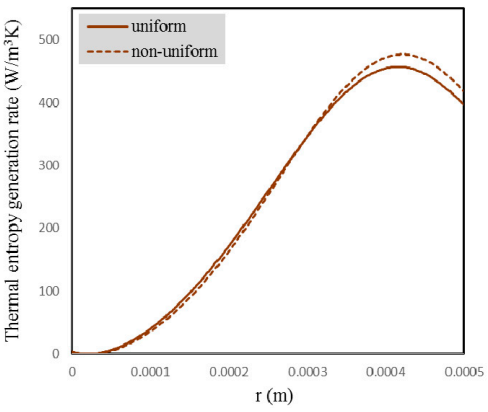

Figure 24. Thermal entropy generation rate for two uniform and non-uniform models at φ_m = 5%, Re = 2000, and d_p = 90 nm.

Figure 25 demonstrates the frictional entropy generation rate for two models (namely, uniform and non-uniform) at φ_m = 5%, Re = 2000, and d_p = 90 nm. It is seen that taking particle migration into consideration significantly reduces the frictional entropy generation. Figure 26 indicates that, due to migration of the nanoparticles to the central areas and the viscosity increase there, the velocity distribution of the non-uniform model is flatter than that of the uniform model. This leads to the velocity gradient related to the former to be below that of the later near the tube centerline, and thus in these regions, the frictional entropy production rate for the non-uniform model will be lower. Adjacent to the wall, in spite of the higher velocity gradient in the non-uniform model, the frictional entropy generation rate is lower than the one obtained from the uniform model. This is because of the smaller viscosity for the non-uniform model near the wall as a consequence of the particle migration toward the central regions. The discrepancy between the frictional entropy production rates adjacent to the wall for two approaches is approximately 14%, which gradually decreases approaching the centerline.

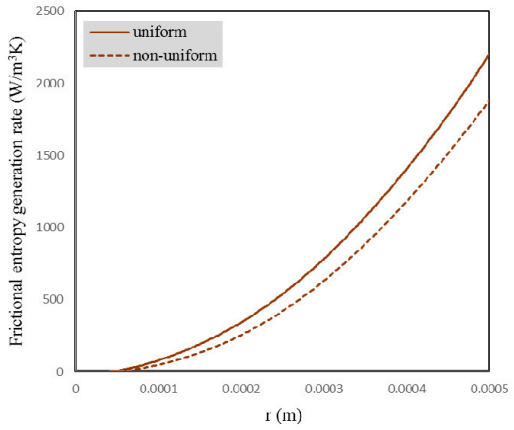

Figure 25. Frictional entropy generation rate for two models (namely, uniform and non-uniform) at φ_m = 5%, Re = 2000, and d_p = 90 nm.

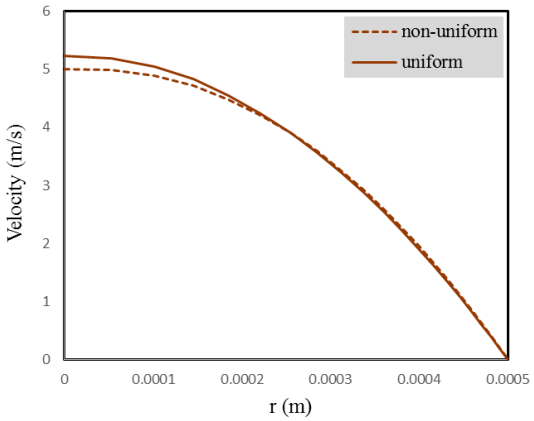

Figure 26. Velocity profiles for uniform and non-uniform models.

Figure 27 compares the total entropy production rates achieved from the uniform and non-uniform models at φ_m = 5%, Re = 2000, and d_p = 90 nm. Under these conditions, since the frictional entropy generation dominates the thermal entropy production, and the frictional entropy production of the uniform model is greater than that of the non-uniform model (Figure 25), the total entropy production for the uniform model is greater than that of the non-uniform model.

Figure 28 illustrates the thermal entropy production rate for the uniform and non-uniform models at two different Reynolds numbers for φ_m = 5% and d_p = 90 nm. It is clear that the discrepancy

between the amounts of thermal entropy production rate obtained from these two models at the higher Reynolds number is greater in comparison with the lower Reynolds number, which is due to higher non-uniformity of concentration at the greater Reynolds number.

Similar to the thermal entropy production, the difference in the frictional entropy production obtained from these two models increases by increasing the Reynolds number (Figure 29).

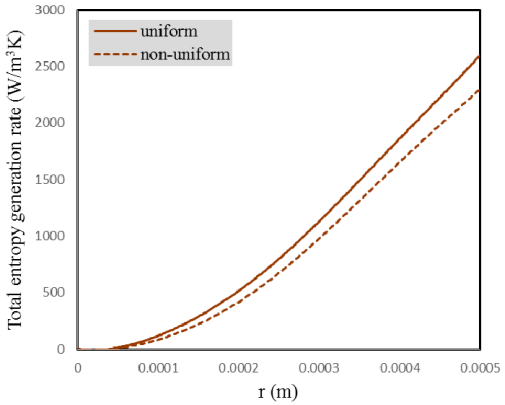

Figure 27. Total entropy generation rates obtained from the uniform and non-uniform models at φ_m = 5%, Re = 2000, and d_p = 90 nm.

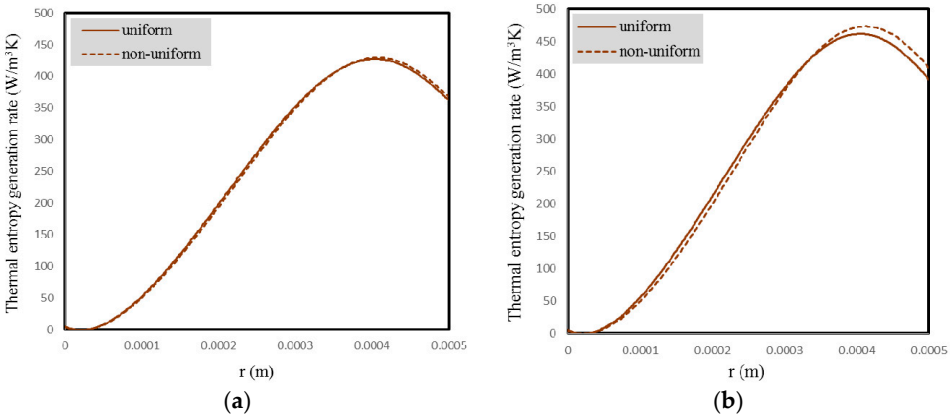

Figure 28. Thermal entropy generation rate obtained from uniform and non-uniform models for φ_m = 5% and d_p = 90 nm at: (**a**) Re = 200; (**b**) Re = 1000.

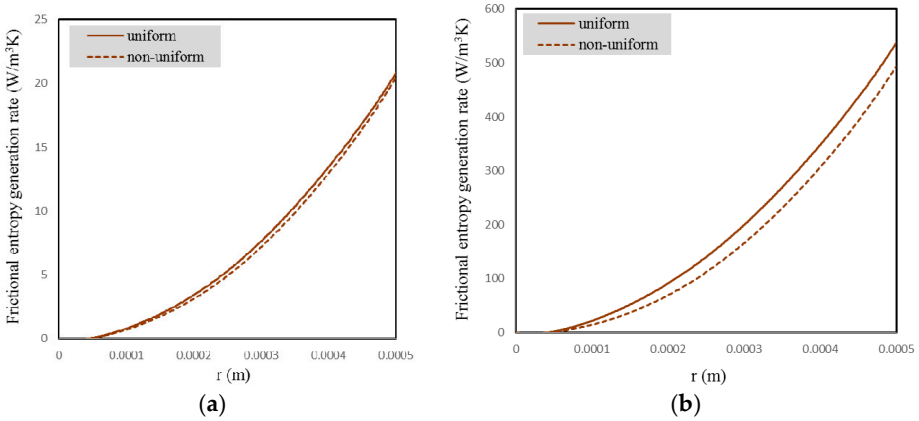

Figure 29. Frictional entropy generation rate obtained from uniform and non-uniform models for φ_m = 5% and d_p = 90 nm at: (**a**) Re = 200; (**b**) Re = 1000.

Figure 30 provides both thermal and frictional entropy generation rates obtained from the uniform model and non-uniform one for the particle size of 10 nm at φ_m = 5% and Re = 2000. As observed in this figure, in contrast with Figures 24 and 25 (which were for the particles of 90 nm), since the particle distribution is very uniform for d_p = 10 nm, no significant difference is noticed between the entropy generation rates of the uniform and non-uniform models. Moreover, a comparison between this figure with Figures 24 and 25 clarifies that the effect of changing the particle size on the difference between the uniform and non-uniform models for frictional entropy production is greater in comparison with thermal entropy production. Based on Figures 24 and 25 (which are depicted for d_p = 90 nm), the difference between the rates of thermal entropy generation obtained from the two models near the wall is about 5%, and the difference between the rates of frictional entropy generation obtained from the two models near the wall is about 14.5%, while these differences are negligible for 10 nm particles, as shown in Figure 30.

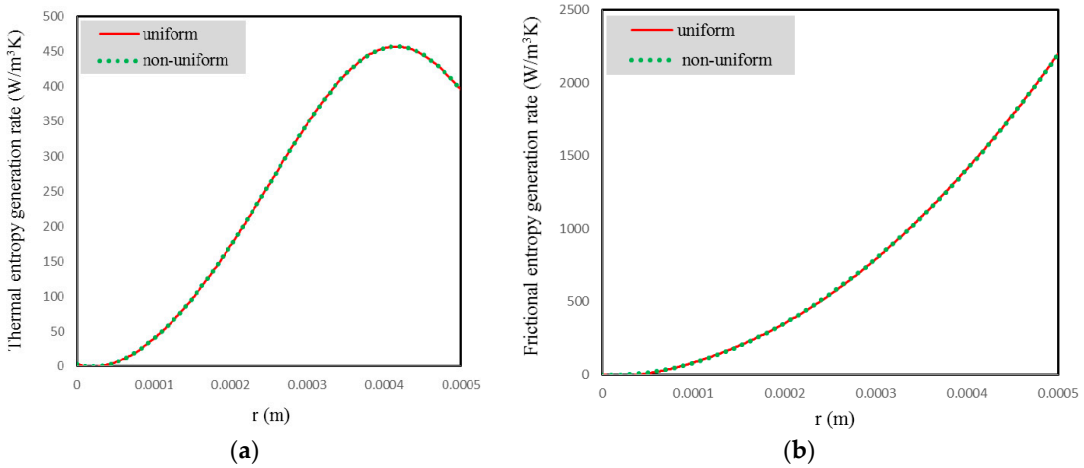

Figure 30. Entropy generation rates obtained from the uniform and non-uniform models for particle size of 10 nm at φ_m = 5% and Re = 2000: (**a**) thermal; (**b**) frictional.

Figure 31 demonstrates the variations of the thermal, frictional, and total entropy production rates of water upon adding particles of 90 nm size with the concentration of 5% at Re = 2000. It is seen that the thermal entropy production rate of the base fluid decreases, and its frictional entropy production rate increases; however, due to the dominance of the latter to the former, the total entropy generation increases.

Figure 32 demonstrates the variations in the thermal, frictional, and total entropy production rates by adding nanoparticles of 90 nm size with the concentration of 5% at Re = 200. As seen from Figure 32c, in contrast to the case of Re = 2000, addition of the nanoparticles reduces the total entropy production rate by about 5.5% for the base fluid. Therefore, from the second law standpoint, in these conditions, the nanofluid will be of lower irreversibility in comparison with the base fluid; thus, it is more optimal than the base fluid for effectual use of the available energy. This is because at this Reynolds number, heat transfer has a greater contribution to the generation of entropy in comparison with the friction, and (as shown in Figure 32a) the rate of thermal entropy production related to the nanofluid is smaller than the water. The addition of nanoparticles to the water will on average multiply the frictional entropy generation rate by approximately four (see Figure 32b), but the rate of thermal entropy generation decreases by about 7.5%, and finally, the total entropy production decreases as a result of higher contribution of the thermal entropy production.

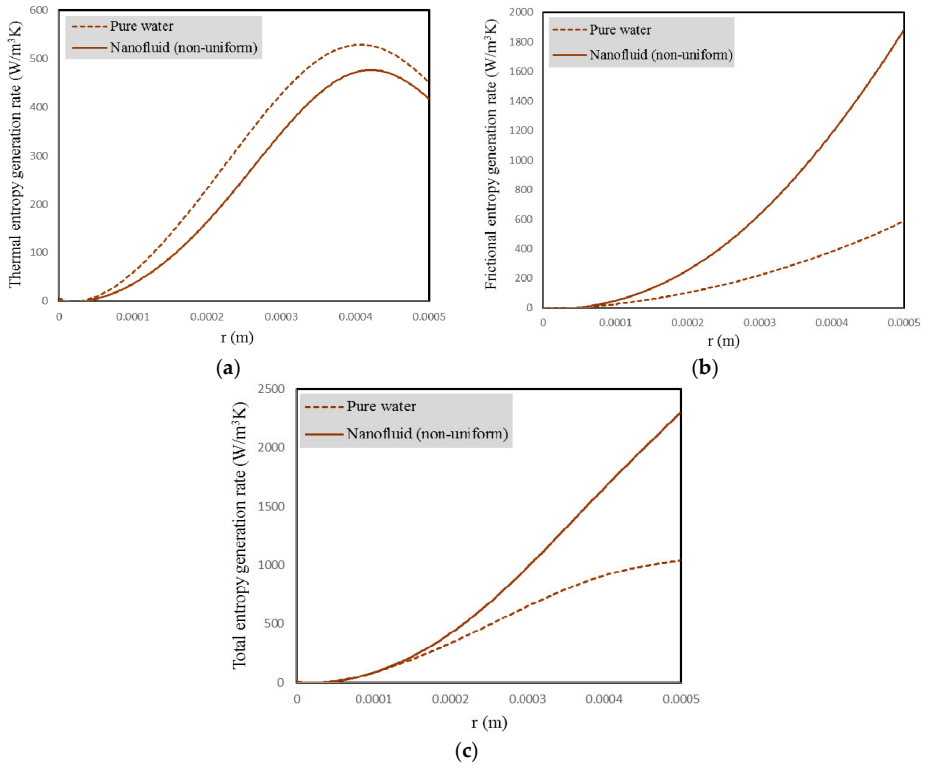

Figure 31. Variations of entropy generation rates of base fluid upon adding particles of 90 nm size with concentration of 5% at *Re* = 2000: (**a**) thermal; (**b**) frictional; (**c**) total.

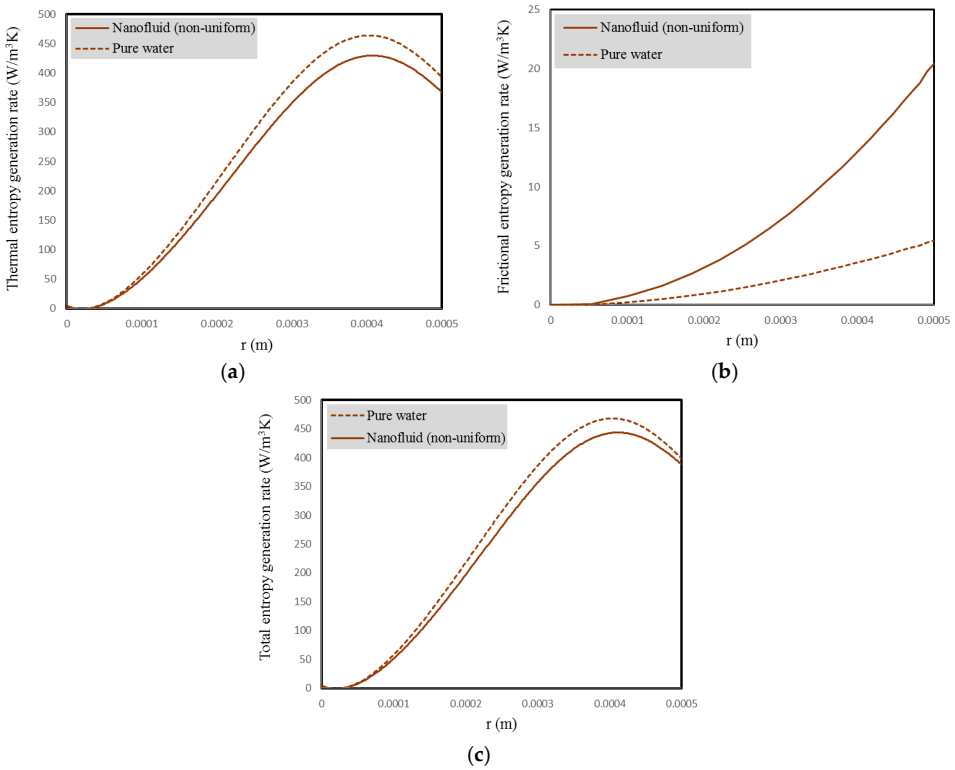

Figure 32. Variations of entropy generation rates of base fluid upon adding particles of 90 nm size with concentration of 5% at *Re* = 200: (**a**) thermal; (**b**) frictional; (**c**) total.

In the following, the entropy generated in the total volume of the nanofluid will be evaluated and discussed under different conditions. These values are obtained by integrating over the entire domain of the nanofluid, according to Equation (27).

Figure 33 illustrates the rates of thermal, frictional, and total entropy production for different concentrations at Re = 2000 and d_p = 90 nm for two states with and without the migration of nanoparticles (i.e., uniform and non-uniform models). It is seen that for the two models, augmenting the concentration decreases the thermal entropy production and raises the frictional entropy production, such that by increasing the concentration from 1% to 5% for the non-uniform model, the rate of thermal entropy production reduces by about 14%, whereas the rate of frictional entropy production augments by about 120%. It causes the total entropy production increment rate to 73%. It is also obvious from Figure 33 that at the low concentration, since the particle distribution is almost uniform, there would be no significant difference between the data achieved from the uniform model and the non-uniform one. However, at the higher concentrations, the difference between the results of these two models increases. Therefore, for the 5% concentration, the frictional and thermal entropy generation rates obtained from the non-uniform model will be around 16% and 3% lower and higher, respectively, than those of the uniform model. Therefore, the results of the uniform model are acceptable only at low concentrations. Meanwhile, by considering particle migration, a lower total entropy production rate will be obtained as compared to the uniform model.

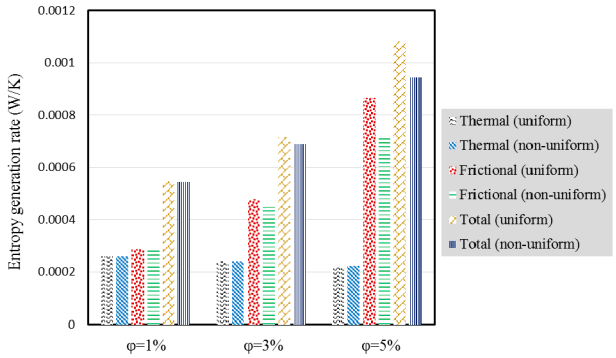

Figure 33. Entropy generation rates for different concentrations at Re = 2000 and d_p = 90 nm for two cases with and without particle migration (non-uniform and uniform, respectively).

Table 3 lists the rates of thermal, frictional, and total entropy production at φ_m = 5% and d_p = 90 nm for the uniform and non-uniform models at different Reynolds numbers. It is noticed that augmenting the Reynolds number decreases the rate of thermal entropy production and raises the rate of frictional entropy production for both models. Increase of the frictional entropy production rate occurs more considerably than the decrease of the thermal entropy production rate. Meanwhile, for smaller Reynolds numbers, great discrepancy is not seen between the results of the uniform model and the non-uniform one, though this difference becomes more considerable at greater Reynolds numbers. As discussed earlier, it is because the particle migration happens more significantly at the higher Reynolds numbers.

Table 3. Entropy generation rates at φ_m = 5% and d_p = 90 nm for the uniform and non-uniform models at various Reynolds numbers.

Re	Entropy Generation Rate (Uniform Model) W/K			Entropy Generation Rate (with Particle Migration) W/K		
	Thermal	**Frictional**	**Total**	**Thermal**	**Frictional**	**Total**
200	0.0002655	8.43×10^{-6}	0.0002740	0.0002656	8.11×10^{-6}	0.0002737
1000	0.0002489	0.0002155	0.0004645	0.0002514	0.0001887	0.0004401
2000	0.0002174	0.0008647	0.0010823	0.0002230	0.0007202	0.0009432

To evaluate the contributions of two factors in the total entropy production, the Bejan number is presented in Table 4 for two models at φ_m = 5% and d_p = 90 nm for different Reynolds numbers. It is obvious that the Bejan number reduces for greater Reynolds numbers, which indicates a decrease of the heat transfer contribution in comparison with the friction. At Re = 200, more than 90% of the entropy generation is originated from heat transfer, while the heat transfer contribution is about 20% at Re = 2000. For the case of considering particle migration, a greater Bejan number is obtained in comparison with the uniform model. Therefore, in this case, the heat transfer contribution is more significant in comparison with the uniform model. This becomes even more significant at higher Reynolds numbers.

Table 4. Bejan number for two models at φ_m = 5% and d_p = 90 nm for various Reynolds numbers.

Re	Uniform Model	With Particle Migration
200	0.969	0.970
1000	0.536	0.571
2000	0.201	0.236

Figure 34 shows the rates of thermal, frictional, and total entropy production, considering particle migration for various particle sizes at Re = 2000 and φ_m = 5%. It is noticed that the rate of thermal entropy production remains almost constant with changing particle size, since as the particle size changes, the local rate of thermal entropy generation increases in some regions and decreases elsewhere, as shown in Figure 18. Therefore, its global value (which is indicative of the thermal entropy generation throughout the nanofluid domain) remains almost unchanged. Looking at Figure 34 clarifies the fact that the rate of frictional entropy production reduces with particle enlargement, because of the reduction in local rates of frictional entropy production (see Figure 19). In addition, the total entropy production rate decreases with particle enlargement, such that from 10 nm to 90 nm, its value reduces by about 13%.

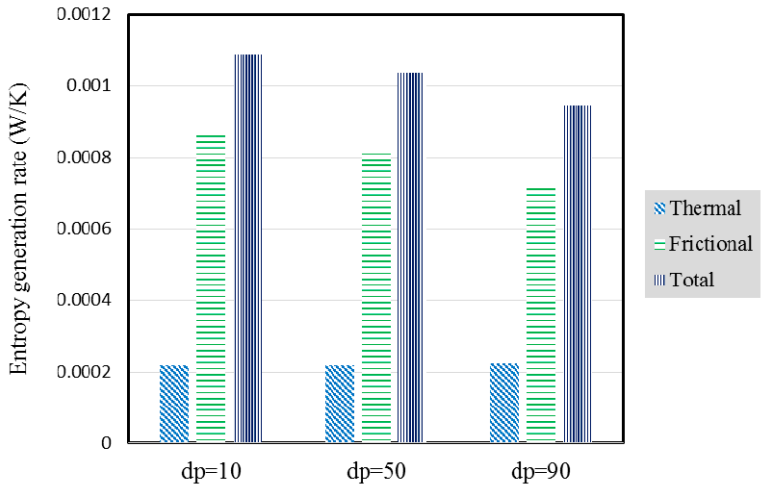

Figure 34. Entropy generation rates considering particle migration at Re = 2000 and φ_m = 5% for different particle sizes.

Applying the second law of thermodynamics, flow of a nanofluid within a minichannel was evaluated in the present survey. However, since most of the conducted investigations on nanofluids have followed the first law of thermodynamics, and since the great importance of the second law of thermodynamics is in the optimization of systems and the efficient use of energy, much more investigations are needed in this area.

7. Conclusions

A second law analysis was carried out in this research by numerical solution using control volume method for the water–alumina nanofluid flow in the laminar regime through a circular minichannel. For this purpose, the entropy generation rates resulting from both heat transfer and friction were evaluated. In the simulations, particle migration was considered to study its effect on the entropy generation. Particle migration led to non-uniform profiles of the thermophysical properties of the nanofluid due to the development of a non-uniformity in the concentration distribution. Thus, it is effective on both velocity and temperature profiles. The entropy generation rates were assessed locally and globally (integrated). At the higher Reynolds numbers, greater concentrations, and larger particle sizes, the particle migration involved a more considerable influence on the entropy production, since the non-uniformity in the properties' distribution was intensified. For investigation of the rates of local entropy production, the profiles of thermophysical properties and velocity were analyzed. The results indicated that in some conditions, by adding the nanoparticles to the water, the rate of total entropy production decreases, which is a beneficial occurrence for effectual utilization of energy. For the case considering particle migration, a greater Bejan number was obtained in comparison with the uniform model. Therefore, in this case, the heat transfer contribution is more significant in comparison with the uniform model.

Acknowledgments: The authors gratefully acknowledge the editor and three anonymous reviewers for their helpful comments for the improvement of this paper.

Author Contributions: Mehdi Bahiraei carried out the analyses and wrote the manuscript. Navid Cheraghi Kazerooni performed the numerical simulations and computer runs. Both authors have read and approved the final manuscript.

Conflicts of Interest: The authors declare no conflict of interest.

References

1. Shahrul, I.M.; Mahbubul, I.M.; Saidur, R.; Khaleduzzaman, S.S.; Sabri, M.F.M.; Rahman, M.M. Effectiveness study of a shell and tube heat exchanger operated with nanofluids at different mass flow rates. *Numer. Heat Transf. Part A Appl.* **2014**, *65*, 699–713. [CrossRef]
2. Bahiraei, M.; Hangi, M.; Saeedan, M. A novel application for energy efficiency improvement using nanofluid in shell and tube heat exchanger equipped with helical baffles. *Energy* **2015**, *93*, 2229–2240. [CrossRef]
3. Alizad, K.; Vafai, K.; Shafahi, M. Thermal performance and operational attributes of the startup characteristics of flat-shaped heat pipes using nanofluids. *Int. J. Heat Mass Transf.* **2012**, *55*, 140–155. [CrossRef]
4. Chen, Y.J.; Wang, P.Y.; Liu, Z.H. Application of water-based SiO_2 functionalized nanofluid in a loop thermosyphon. *Int. J. Heat Mass Transf.* **2013**, *56*, 59–68. [CrossRef]
5. Leong, K.Y.; Saidur, R.; Kazi, S.N.; Mamun, A.H. Performance investigation of an automotive car radiator operated with nanofluid-based coolants (nanofluid as a coolant in a radiator). *Appl. Therm. Eng.* **2010**, *30*, 2685–2692. [CrossRef]
6. Bahiraei, M.; Hangi, M. Flow and heat transfer characteristics of magnetic nanofluids: A review. *J. Magn. Magn. Mater.* **2015**, *374*, 125–138. [CrossRef]
7. Duangthongsuk, W.; Dalkilic, A.S.; Wongwises, S. Convective heat transfer of Al_2O_3–water nanofluids in a microchannel heat sink. *Curr. Nanosci.* **2012**, *8*, 317–322. [CrossRef]
8. Yousefi, T.; Veysi, F.; Shojaeizadeh, E.; Zinadini, S. An experimental investigation on the effect of Al_2O_3–H_2O nanofluid on the efficiency of flat-plate solar collectors. *Renew. Energy* **2012**, *39*, 293–298. [CrossRef]
9. Sheremet, M.A.; Pop, I.; Shenoy, A. Unsteady free convection in a porous open wavy cavity filled with a nanofluid using Buongiorno's mathematical model. *Int. Commun. Heat Mass Transf.* **2015**, *67*, 66–72. [CrossRef]
10. Hedayati, F.; Domairry, G. Nanoparticle migration effects on fully developed forced convection of TiO_2–water nanofluid in a parallel plate microchannel. *Particuology* **2016**, *24*, 96–107. [CrossRef]

11. Sheremet, M.A.; Pop, I. Natural convection in a wavy porous cavity with sinusoidal temperature distributions on both side walls filled with a nanofluid: Buongiorno's mathematical model. *J. Heat Transf.* **2015**, *137*, 072601. [CrossRef]
12. Masuda, H.; Ebata, A.; Teramae, K.; Hishinuma, N. Alteration of thermal conductivity and viscosity of liquid by dispersing ultra-fine particles (dispersion of Al_2O_3, SiO_2 and TiO_2 ultra-fine particles). *Netsu Bussei* **1993**, *4*, 227–233. [CrossRef]
13. Choi, S.U.S.; Eastman, J.A. Enhanced Heat Transfer Using Nanofluids. U.S. Patent, 6,221,275 B1, 24 April 2001.
14. Eastman, J.A.; Choi, S.U.S.; Li, S.; Yu, W.; Thomson, L.J. Anomalously increased effective thermal conductivities of ethylene glycol based nanofluids containing copper nanoparticles. *Appl. Phys. Lett.* **2001**, *78*, 718–720. [CrossRef]
15. Malvandi, A.; Ganji, D.D. Effects of nanoparticle migration and asymmetric heating on magnetohydrodynamic forced convection of alumina/water nanofluid in microchannels. *Eur. J. Mech. B Fluids* **2015**, *52*, 169–184. [CrossRef]
16. Bahiraei, M. A comprehensive review on different numerical approaches for simulation in nanofluids: Traditional and novel techniques. *J. Dispers. Sci. Technol.* **2014**, *35*, 984–996. [CrossRef]
17. Garoosi, F.; Bagheri, G.; Rashidi, M.M. Two phase simulation of natural convection and mixed convection of the nanofluid in a square cavity. *Powder Technol.* **2015**, *275*, 239–256. [CrossRef]
18. Sundar, S.; Sharma, K.V. Turbulent heat transfer and friction factor of Al_2O_3 nanofluid in circular tube with twisted tape inserts. *Int. J. Heat Mass Transf.* **2010**, *53*, 1409–1416. [CrossRef]
19. Mahdavi, M.; Sharifpur, M.; Meyer, J.P. CFD modelling of heat transfer and pressure drops for nanofluids through vertical tubes in laminar flow by Lagrangian and Eulerian approaches. *Int. J. Heat Mass Transf.* **2015**, *88*, 803–813. [CrossRef]
20. Malvandi, A.; Moshizi, S.A.; Ganji, D.D. Effects of temperature-dependent thermophysical properties on nanoparticle migration at mixed convection of nanofluids in vertical microchannels. *Powder Technol.* **2016**, *303*, 7–19. [CrossRef]
21. Fazeli, H.; Madani, S.; Mashaei, P.R. Nanofluid forced convection in entrance region of a baffled channel considering nanoparticle migration. *Appl. Therm. Eng.* **2016**, *106*, 293–306. [CrossRef]
22. Zhu, J.; Yang, D.; Zheng, L.; Zhang, X. Effects of second order velocity slip and nanoparticles migration on flow of Buongiorno nanofluids. *Appl. Math. Lett.* **2016**, *52*, 183–191. [CrossRef]
23. Ding, Y.; Wen, D. Particle migration in a flow of nanoparticle suspensions. *Powder Technol.* **2005**, *149*, 84–92. [CrossRef]
24. Bahiraei, M. Effect of particle migration on flow and heat transfer characteristics of magnetic nanoparticle suspensions. *J. Mol. Liq.* **2015**, *209*, 531–538. [CrossRef]
25. Malvandi, A.; Ghasemi, A.; Ganji, D.D. Thermal performance analysis of hydromagnetic Al_2O_3-water nanofluid flows inside a concentric microannulus considering nanoparticle migration and asymmetric heating. *Int. J. Therm. Sci.* **2016**, *109*, 10–22. [CrossRef]
26. Bejan, A. A Study of entropy generation in fundamental convective heat transfer. *ASME J. Heat Transf.* **1979**, *101*, 718–725. [CrossRef]
27. Bejan, A. *Entropy Generation Minimization*; CRC Press: Boca Raton, FL, USA, 1996.
28. Moghaddami, M.; Mohammadzade, A.; Varzane Esfehani, S.A. Second law analysis of nanofluid flow. *Energy Convers. Manag.* **2011**, *52*, 1397–1405. [CrossRef]
29. Sheremet, M.A.; Oztop, H.F.; Pop, I.; Abu-Hamdeh, N. Analysis of entropy generation in natural convection of nanofluid inside a square cavity having hot solid block: Tiwari and Das' model. *Entropy* **2016**, *18*, 9. [CrossRef]
30. Mahian, O.; Mahmud, S.; Wongwises, S. Entropy generation between two rotating cylinders in the presence of magnetohydrodynamic flow using nanofluids. *J. Thermophys. Heat Transf.* **2013**, *27*, 161–169. [CrossRef]
31. Boghrati, M.; Ebrahimnia Bajestan, E.; Etminan, V. Entropy generation minimization of confined nanofluids laminar flow around a block. In Proceedings of the 10th Biennial Conference on Engineering Systems and Analysis ESDA2010, Istanbul, Turkey, 12–14 July 2010.
32. Mahmoudi, A.H.; Shahi, M.; Pop, I.; Talebi, F. MHD natural convection and entropy generation in a trapezoidal enclosure using Cu–water nanofluid. *Comput. Fluids* **2013**, *72*, 46–62. [CrossRef]
33. Leighton, D.; Acrivos, A. The shear-induced migration of particles in concentrated suspensions. *J. Fluid Mech.* **1987**, *181*, 415–439. [CrossRef]

34. Phillips, R.J.; Armstrong, R.C.; Brown, R.A.; Graham, A.L.; Abbott, J.R. A constitutive equation for concentrated suspensions that accounts for shear-induced particle migration. *Phys. Fluids A* **1992**, *4*, 30–40. [CrossRef]
35. Liu, S. Particle dispersion for suspension flow. *Chem. Eng. Sci.* **1999**, *54*, 873–891. [CrossRef]
36. Maiga, S.; Palm, S.J.; Nguyen, C.T.; Roy, G.; Galanis, N. Heat transfer enhancement by using nanofluids in forced convection flows. *Int. J. Heat Fluid Flow* **2005**, *26*, 530–546. [CrossRef]
37. Bejan, A.; Kraus, A.D. *Heat Transfer Handbook*; John Wiley and Sons: New York, NY, USA, 2003.
38. Bahiraei, M.; Hosseinalipour, S.M. Thermal dispersion model compared with Euler-Lagrange approach in simulation of convective heat transfer for nanoparticle suspensions. *J. Dispers. Sci. Technol.* **2013**, *34*, 1778–1789. [CrossRef]